Journal of
Materials Chemistry A

ROYAL SOCIETY
OF CHEMISTRY

PAPER

View Article Online
View Journal

Check for updates

Cite this: DOI: 10.1039/d6ta01917j

MFU-4 as a benchmark molecular sieve for efficient CO_2/CH_4 separation in biogas upgrading

Adriano Henrique,[a] Prantar Dutta,[bc] Mayank Gupta,[d] Georges Mouchaham, *[d] Yann Magnin,[c] Christian Serre, [d] Guillaume Maurin *[be] and José A. C. Silva*[a]

Received 4th March 2026
Accepted 22nd May 2026

DOI: 10.1039/d6ta01917j

rsc.li/materials-a

The efficient separation of CO_2 from CH_4 is central to industrial biogas upgrading for the production of pipeline-quality biomethane. Kinetic, molecular sieve-based adsorption is preferred over thermodynamic approaches, making small-pore adsorbents such as CMS-3K and ion-exchanged ETS-4 the current industrial standard. Here, we show, through a combination of breakthrough experiments and computational analysis, that the ultra-microporous Zn triazolate MOF MFU-4 significantly surpasses these benchmarks. Its unique architecture, featuring alternating small and large cages connected by narrow, square-shaped pore gates, kinetically hinders CH_4 diffusion while facilitating rapid CO_2 transport and achieving high CO_2 uptake, effectively overcoming the long-standing trade-off between CO_2/CH_4 selectivity and CO_2 capacity. As a result, MFU-4 achieves CO_2/CH_4 kinetic selectivity up to twice that of ETS-4 and four times that of CMS-3K, with CO_2 working capacities up to seven and four times higher, respectively, over the 100–500 kPa range, and an exceptional CO_2 uptake of ~7.4 mol kg^{-1} at 298 K and 500 kPa. These findings establish MFU-4 as an excellent molecular sieve for biogas upgrading, delivering performance far beyond current industrial standards.

1 Introduction

The upgrading of biogas, primarily a mixture of methane (CH_4) and carbon dioxide (CO_2), into pipeline-quality biomethane, a high-value natural-gas substitute, has emerged as a critical process for both renewable energy production and greenhouse-gas mitigation.[1,2] Efficient removal of CO_2 from the CH_4-rich stream not only enhances the calorific value of the purified gas but also decreases volumetric flow, thereby, reducing transportation and compression costs while facilitating downstream processing and handling.[3,4] With the growing pressure on circular economy principles and low-carbon energy solutions, adsorption-based technologies for CO_2/CH_4 separation have garnered substantial attention as energy-efficient alternatives to conventional energy-intensive approaches such as water scrubbing, amine absorption and cryogenic processes.[4–6]

In this context, several adsorbent materials have been explored for CO_2/CH_4 separation, predominantly leveraging thermodynamic (equilibrium-driven) selectivity, where CO_2 is preferentially adsorbed due to its high polarizability and quadrupole moment which promote stronger interactions with the host frameworks compared to CH_4. Among these, zeolites such as 13X,[7–14] 4A,[11,15–18] 5A,[19–22] together with a wide variety of ion-exchanged derivatives,[23–32] have long been regarded as benchmark adsorbents. Their prominence arises from well-defined microporous frameworks and strong CO_2 affinity, which arises from specific interactions between CO_2 molecules and extra-framework cations, as well as from confinement effects within their uniform pore structures. More recently, metal–organic frameworks (MOFs)[33] have emerged as highly tunable alternative porous adsorbents, offering the unprecedented ability to precisely tailor pore size, shape and chemical functionality to enhance interactions with CO_2. Representative examples include extended MOF-74 and its amine-grafted frameworks,[34–40] which exhibit high CO_2 uptake due to strong interactions with open metal sites and/or amine functionalities, as well as small-pore MOFs such as MIL-120(Al),[41–43] CALF-20(Zn),[44] and NbOFFIVE-1-Ni,[45] where CO_2 affinity is largely governed by molecular confinement within the pores.

Despite its advantages, this equilibrium-based adsorption strategy often entails substantial energy penalties during adsorbent regeneration and may lead to diminished CH_4 recovery, particularly under cyclic operation. In such cases, processes such as Vacuum Pressure Swing Adsorption (VPSA) are typically required to fully regenerate and reset the adsorption bed, further increasing operational complexity and energy demand. These limitations highlight the need for the development of next-generation adsorbents and separation strategies that

---

[a] CIMO, La SusTEC, Instituto Politécnico de Bragança, Campus Santa Apolónia, 5300-253 Bragança, Portugal. E-mail: jsilva@ipb.pt
[b] ICGM, Université de Montpellier, CNRS, ENSCM, Montpellier 34293, France. E-mail: guillaume.maurin1@umontpellier.fr
[c] OneTech, R&D, CSTJF, TotalEnergies, Pau 64018, France
[d] Institut des Matériaux Poreux de Paris, ESPCI Paris, Ecole Normale Supérieure, CNRS, PSL University, Paris 75005, France. E-mail: georges.mouchaham@ens.psl.eu
[e] Institut Universitaire de France, France

simultaneously deliver high selectivity, low regeneration energy requirements, and robust operational stability, thereby enabling more sustainable and economically viable biogas upgrading processes. Accordingly, kinetic separation mechanisms offer an attractive alternative to purely equilibrium-driven strategies. In this approach, selectivity originates from differences in diffusion rates or mass-transfer kinetics, driven by variations in adsorption strength and/or steric constraints imposed by the pore dimensions relative to molecular size. Faster-diffusing species are preferentially transported, enabling operation at high feed velocities and short cycle times. Importantly, because CH_4 is only weakly adsorbed, regeneration requirements are significantly reduced, lowering purge demand and overall energy consumption.[46,47] As a result, CH_4 can be efficiently recovered in the raffinate stream with minimal losses to the adsorbent phase.

In this context, two materials have emerged as industrial benchmarks, illustrating the practical viability of diffusion-controlled separations for scalable biogas upgrading. The first is the carbon molecular sieve CMS-3K (commercially supplied by Takeda/Osaka Gas), which displays rapid CO_2 adsorption, whereas CH_4 uptake can require several days to reach equilibrium, reflecting pronounced kinetic hindrance for CH_4 diffusion.[48,49] This behavior originates from the ultra-small pore entrances of CMS-3K, whose dimensions closely approach the kinetic diameter of CH_4, thereby imposing a strong mass-transfer resistance at the micropore apertures. CMS materials are currently deployed in industrial VPSA processes, including the METHAGEN systems commercialized by SysAdvance.[50,51] The second benchmark material, the zeotype ETS-4 (Engelhard Titanosilicate-4), modified with alkaline-earth cations, similarly exploits precise pore-aperture tuning to introduce diffusion barriers or molecular sieving effects that restrict CH_4 while favouring smaller or more rapidly diffusing species such as N_2 or CO_2.[52–56] ETS-4 is widely implemented under the Molecular Gate® technology, a registered trademark of BASF Catalysts LLC and exclusively licensed to Guild Associates.[57] Despite their clear industrial relevance, both materials exhibit relatively modest equilibrium CO_2 adsorption capacities (<3 mol kg^{-1} at 500 kPa).[48,49,56] Consequently, deep vacuum levels (10–20 kPa) are required during regeneration to achieve practical working capacities.[58] This dependence on vacuum-intensive operation increases energy demand and process complexity, elevating both capital and operating expenditures (CAPEX and OPEX) and ultimately limiting overall process efficiency.

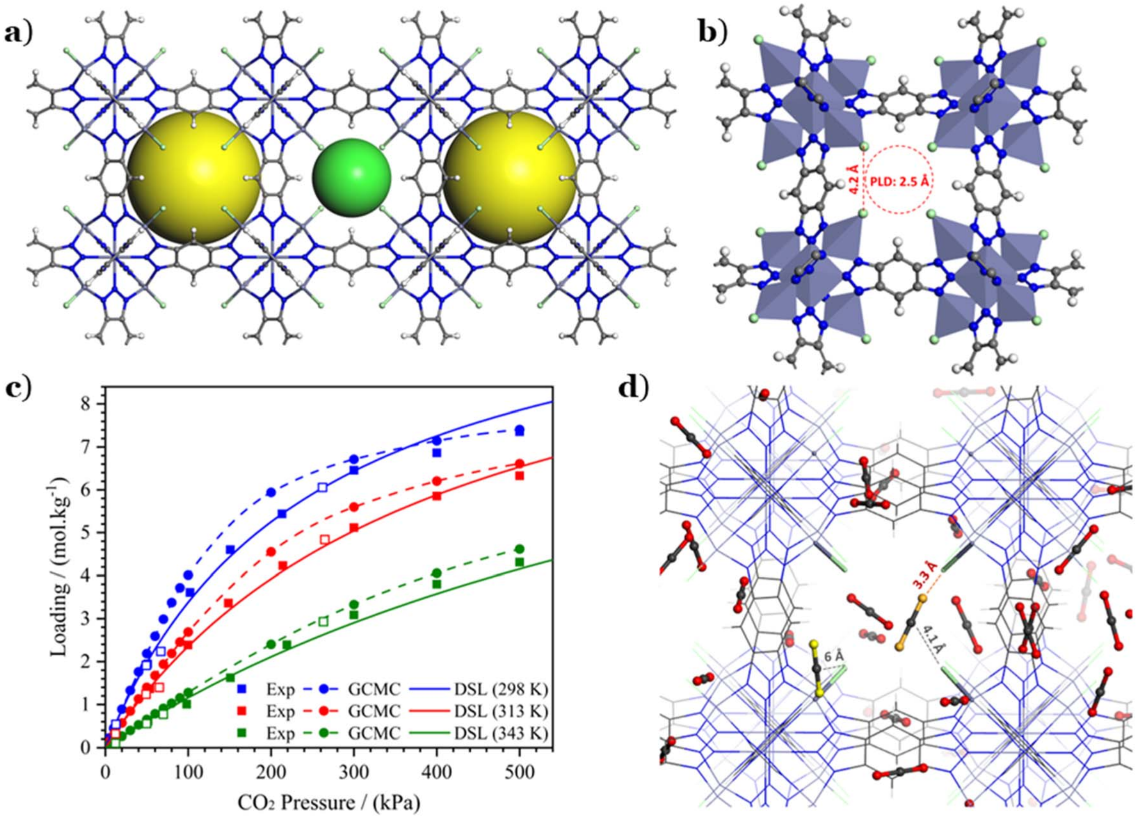

Fig. 1 (a) Pore network of MFU-4 with alternating large (yellow spheres) and small (green sphere) cages. (b) Square-shaped pore gate, with pore limiting diameter of 2.5 Å, separating the cages. (c) Equilibrium single-component CO_2 adsorption isotherms on MFU-4 in the temperature range of 298–343 K. Filled symbols: single-component experimental data; open symbols: CO_2 loadings obtained from binary breakthrough experiments; symbols and dashed: GCMC simulations; continuous lines: DSL thermodynamic model fit. (d) Microscopic mechanism of CO_2 adsorption in MFU-4 illustrated by a representative GCMC snapshot from simulations at 100 kPa. Two CO_2 molecules with the shortest MOF-CO_2 distances for each adsorption site are highlighted—one adsorbed at the pore gate (O_{CO_2} in orange; Cl–C_{CO_2} distance: 4.1 Å) and one located inside the large cage (O_{CO_2} in yellow; Cl–C_{CO_2} distance: 6 Å).

To overcome these limitations and move beyond the intrinsic trade-off between CO_2/CH_4 kinetic selectivity and CO_2 uptake, alternative classes of materials must be explored. In this regard, ultra-small pore MOFs offer a unique platform to transcend this long-standing compromise, enabling the rational design of diffusion barriers or dynamic pore-gating mechanisms that selectively regulate molecular transport, enabling rapid CO_2 diffusion while kinetically restricting CH_4, all without sacrificing adsorption capacity within larger internal cavities. Guided by this design principle, we conducted a systematic examination of MOF structural databases and identified MFU-4(Zn)[59] (Metal–Organic Framework Ulm University-4) as a particularly promising candidate. Its framework, constructed from Zn-based secondary building units interconnected by benzo[1,2-*d*:4,5-*d′*]bistriazolate ligands, features an alternating arrangement of small (~4 Å) and large (~12 Å) cages interconnected through ultranarrow, square-shaped pore apertures delimited by four chloride atoms with a limiting diameter of approximately 2.5 Å (Fig. 1a and b). This precise integration of confined apertures and spacious cavities creates an architecture ideally suited to impose strong kinetic constraints on CH_4 diffusion while maintaining fast CO_2 transport and high CO_2 uptake within the larger cages.

To validate this concept, we employed a synergistic combination of advanced breakthrough experiments and computational methods, demonstrating that MFU-4(Zn) surpasses the industrial benchmark adsorbents CMS-3K and ETS-4 in CO_2/CH_4 separation.

2 Methodology

2.1 Synthesis and characterization

2.1.1 Synthesis. The H_2-BBTA linker was synthesized according to previously reported procedures, starting from 1,5-dichloro-2,4-dinitrobenzene.[59,60] MFU-4 was synthesized in solvothermal conditions by dissolving anhydrous $ZnCl_2$ (136 mg, 1.00 mmol) and H_2-BBTA (40 mg, 0.25 mmol) in 4 mL of DMF, transferring the solution to a screw-capped glass pressure tube, and heating at 140 °C for 3 days, followed by cooling to room temperature. The supernatant was removed, and the yellow microcrystalline solid was washed with DMF (3 × 1 mL) and dried in air to afford 65 mg (≈0.056 mmol, 28%) of MFU-4. The product consisted mainly of cubic microcrystals, with a smaller fraction of octahedral crystals, as observed by SEM (see Discussion below).

2.1.2 Characterization. The FT-IR spectrum of the non-activated pristine MFU-4 confirms the successful formation of the Zn–bistriazolate framework and provides clear evidence for the presence of residual guest molecules within the pores (Fig. S1). In particular, a strong absorption band at ~1652 cm^{-1} is assigned to the C=O stretching vibration of DMF, indicating that DMF molecules remain confined within the framework after synthesis. Additional bands at ~2918 and ~2848 cm^{-1} corresponding to aliphatic C–H stretching further support the presence of occluded solvent molecules (see Section S1.1.1).

The phase purity of the synthesized MFU-4 was confirmed by powder X-ray diffraction (PXRD). The PXRD pattern of the as-synthesized MFU-4 matches well with the simulated pattern generated from the reported single-crystal structure, with all characteristic reflections appearing at the same 2θ positions (Fig. S2). PXRD patterns recorded for materials after activation and CO_2 adsorption remain the same as the pristine material indicating that MFU-4 maintains its structural integrity and exhibits excellent stability (Fig. S3).

The scanning electron microscopy (SEM) images of the as-synthesized MFU-4 (Fig. S4) reveal the presence of well-faceted microcrystalline particles exhibiting two distinct morphologies, namely predominantly blocky/cubic-shaped crystals together with a smaller fraction of octahedral crystallites. These morphologies are identified based on their characteristic geometrical features and faceted structures observed in SEM, which reflect different crystal growth habits under solvothermal conditions. The particle size lies in the micrometer range (~0.5–5 μm), with most crystals typically between 1–3 μm. While an accurate quantitative phase fraction cannot be extracted from SEM images, the cubic morphology is clearly dominant, with octahedral crystals present in lower proportion. To further confirm that both morphologies correspond to the same phase, energy-dispersive X-ray (EDX) analysis was performed on individual crystals. The measured Zn and Cl atomic percentages (Zn ≈ 52.53 at%, Cl ≈ 47.47 at%) correspond to Zn : Cl ratios of ~1 : 0.85 and ~1.09 for cubic and octahedral crystals, respectively, which are in good agreement with the expected MFU-4 stoichiometry. This confirms that both morphologies belong to the same framework rather than different phases or impurities.

Thermogravimetric analysis (TGA) was performed to evaluate the purity, thermal behavior, and guest (DMF) content of MFU-4 in its as-synthesized form. The TGA profile exhibits a characteristic multistep weight-loss behavior consistent with previous reports and aligns well with the formulation $[Zn_5Cl_4(BBTA)_3]\cdot 3DMF\cdot 6H_2O$ (Fig. S5). Three distinct weight-loss steps are observed. An initial weight loss of ~9 wt% below ~80 °C is attributed to the removal of surface-adsorbed moisture and residual lattice water. A second weight loss of ~18 wt% in the temperature range of 120–300 °C corresponds to the release of approximately three DMF molecules per formula unit, in good agreement with the theoretical DMF content (~17.18 wt%), confirming that the as-synthesized material is obtained in a solvated state. At higher temperatures (above ~420 °C), a major weight loss (~49 wt%) is observed due to framework decomposition. After activation at 250 °C, the TGA curves recorded for MFU-4 following CO_2 and N_2 sorption measurements (Fig. S6) differ significantly from those of the as-synthesized sample. In particular, the characteristic weight loss associated with DMF in the 120–300 °C range disappears, confirming the complete removal of pore-confined solvent molecules and the formation of the desolvated framework. However, a low-temperature weight loss remains and is significantly increased. This behavior arises from the re-adsorption of moisture upon exposure of the activated sample to ambient air. Once DMF is removed, the internal pore volume becomes fully accessible, enhancing the affinity of the framework toward water. Quantitatively, the low-temperature weight loss increases from ~9 wt% in the as-synthesized sample to approximately 25–27 wt% in the activated sample, clearly indicating substantial water uptake after activation. This increase reflects the replacement of DMF by adsorbed water molecules within the accessible pores. Importantly, the absence of the intermediate weight-loss step confirms that no DMF remains after activation, and the observed low-temperature loss is solely due to physically adsorbed moisture. This behavior is consistent with literature reports on activated MOFs, where exposure to air leads to rapid water uptake and increased low-temperature mass loss (see Section S1.1.4).

2.2 Fixed bed breakthrough experiments

The single-component adsorption equilibrium data of CO_2 was measured using a chromatographic technique based on dynamic fixed-bed breakthrough experiments. The experimental setup comprises three main sections: (1) gas preparation, (2) adsorption, and (3) analysis. In the gas preparation section, he carrier gas and CO_2 were fed through mass flow controllers, while system pressure was set by back-pressure regulators. The adsorption section contained a stainless-steel column filled with the agglomerated MFU-4 and placed inside a temperature-controlled water bath. The outlet from the fixed bed was directed to the analytical section, where a gas chromatograph equipped with a thermal conductivity detector (TCD) which continuously monitored the CO_2 concentration. For CO_2/CH_4 binary breakthrough experiments, the same procedure was applied. In this case, the feed gas mixture was set in the gas preparation section, and a pre-programmed six-port valve periodically directed aliquots of the outlet stream to a packed column for peak separation before analysis by the TCD detector. Further details on the setup, procedure, and operating conditions are provided in the SI.

2.3 Modelling and numerical simulations

The Aspen Adsorption v11 package[61] was employed to numerically simulate the binary breakthrough experiments. Input data for these simulations were obtained from adsorption equilibrium data (experimental for CO_2 and simulated for CH_4), modelled using the Dual-Site Langmuir (DSL) isotherm.[62] To analyze mass transfer kinetics, a linear driving force (LDF) model was applied,[63] which is based on the solid-phase concentration gradient and has been satisfactorily validated in previous studies.[64,65] Complete details of the assumptions, model equations, parameter correlations, and numerical procedures used to solve the partial differential equations (PDEs) are provided in the SI.

2.4 Molecular simulations and quantum calculations

The crystal structure of MFU-4 was geometry-optimized using periodic density functional theory (DFT) as implemented in the Vienna *Ab initio* Simulation Package (VASP).[66] Calculations were performed using the Perdew–Burke–Ernzerhof (PBE) exchange–correlation functional[67] in conjunction with projector-augmented wave (PAW) pseudopotentials[68] and Grimme's D3 dispersion correction with Becke–Johnson damping.[69,70] Both atomic positions and lattice parameters were relaxed using the conjugate-gradient algorithm with a plane-wave energy cutoff of 600 eV. Convergence criteria of 10^{-6} eV for the total energy and 0.01 eV $Å^{-1}$ for atomic forces were applied. Brillouin-zone sampling was carried out using a $2 \times 2 \times 2$ Monkhorst–Pack *k*-point mesh.[71] The electronic charge density of the optimized structure was subsequently used to derive atom-centered partial charges using the DDEC6 method, as implemented in the Chargemol package.[72–75]

Grand canonical Monte Carlo (GCMC) simulations were first performed to predict the single component adsorption isotherms of CO_2 and CH_4 in MFU-4 at three temperatures (298 K, 313 K, and 343 K) and pressures up to 500 kPa. CO_2 and CH_4 were modeled using the EPM2 (ref. 76) and TraPPE united-atom[77] force fields, respectively, while Lennard-Jones (LJ) parameters for the framework atoms were taken from the Universal Force Field (UFF).[78] LJ interactions between the adsorbates and the octahedrally coordinated Zn atoms were excluded, as these metal centers are deeply shielded within the Kuratowski-type nodes and are effectively inaccessible to guest molecules. Lorentz–Berthelot mixing rules were applied for cross-interactions. Simulations were performed in a $2 \times 2 \times 2$ supercell, employing a cutoff distance of 12 Å for both van der Waals and electrostatic host–guest interactions. Long-range electrostatic interactions were treated using the Ewald summation method. For each pressure point, 2×10^7 Monte Carlo cycles were used for both equilibration and production. All GCMC simulations were performed using Complex Adsorption and Diffusion Simulation Suite (CADSS).[79] The adsorption enthalpies at zero coverage for CO_2 and CH_4 were also calculated using the revised Widom's test particle insertion method.[80] The LJ parameters and partial charges for the atoms of MFU-4 and both adsorbates are provided in Tables S2 and S3, respectively.

The energy barrier associated with crossing the pore gate of MFU-4, which separates alternating large and small cages, was evaluated for both CO_2 and CH_4 using climbing-image nudged elastic band (CINEB)[81] calculations as implemented in the Quickstep module of the CP2K package.[82] The calculations employed the PBE functional with D3/Becke–Johnson dispersion correction, together with triple-ζ valence polarized (TZVP) Gaussian basis sets[83] and Goedecker–Teter–Hutter (GTH) pseudopotentials[84,85] for all atoms. An auxiliary plane-wave cutoff of 500 Ry was used. To model migration across the pore gate, a supercell containing two unit cells along the *a*-direction was constructed. The initial and final states were generated by placing a single adsorbate molecule (CO_2 or CH_4) on either side of the pore gate, followed by full relaxation of atomic positions. The minimum-energy pathway was resolved using seven intermediate images, with a force convergence criterion of 5×10^{-4} hartree.

3 Results and discussion

The equilibrium single component CO_2 adsorption isotherms of MFU-4 were derived from breakthrough experiments performed at 298 K, 313 K, and 343 K over pressures up to 500 kPa (see Table S4 and Fig. S8). The experimentally obtained equilibrium data are compared with the corresponding GCMC simulated adsorption isotherms in Fig. 1c. At all three temperatures, experimental and simulated isotherms are in good agreement and exhibit a characteristic IUPAC Type I profile typical of microporous adsorbents, with a steep increase in CO_2 uptake at low partial pressures followed by a gradual approach to saturation.[86] The moderately rounded "knee" of the isotherm suggests the presence of more than one adsorption environment. The DSL model provides a robust description of the experimental data over the entire pressure range, indicating that CO_2 adsorption can be rationalized by two families of adsorption sites with comparable affinities but different saturation capacities (see Table S6 for the fitted parameters). This interpretation is supported by the analysis of GCMC configurations which reveals two distinct adsorption sites, one near the Cl atoms delimiting the pore gates and a second situated within the larger cages (Fig. 1d) (see Fig. S10 for more details). The isosteric heat of adsorption (Q_{st}) for CO_2, estimated using the Clausius–Clapeyron relation (Fig. S12), remains essentially constant over the investigated loading range, at $\sim$24.7 kJ mol^{-1} in line with the previously reported experimental values ($\sim$24.4 kJ mol^{-1})[87] and our simulated adsorption enthalpy at infinite dilution ($\sim$24 kJ mol^{-1}).

Adsorption of CH_4 in MFU-4 could not be detected using the flow chromatographic method, most likely due to its extremely slow diffusion within the MOF, resulting in breakthrough times that occur almost simultaneously with the gas residence time in the fixed bed. To validate this hypothesis, DFT-CINEB calculations were performed to quantify the energy barriers for guest migration across the pore gates of MFU-4. Minimum energy pathways (MEPs) were determined by positioning a guest molecule on either side of an individual pore gate as the initial and final states. The resulting MEPs for CH_4 and CO_2 crossing the pore gate are shown in Fig. 2a and b, respectively. CH_4 faces a substantial energy barrier of $\sim$53 kJ mol^{-1}, with a well-defined transition state at the centre of the gate. This large barrier reflects severe steric hindrance, as the spherical CH_4 molecule (kinetic diameter $\sim$3.8 Å) must pass through a square aperture with a pore limiting diameter of only $\sim$2.5 Å. In contrast, the MEP for CO_2 shows the pore gate as a local energy minimum rather than a transition state. The square gate provides confinement-enhanced stabilization for the linear CO_2 molecule, consistent with GCMC simulations that identify the gate region as the primary adsorption site. Transport of CO_2 between adjacent cages is therefore not limited by an enthalpic barrier but is instead controlled by entropic constraints arising from confinement and molecular orientation. These findings suggest

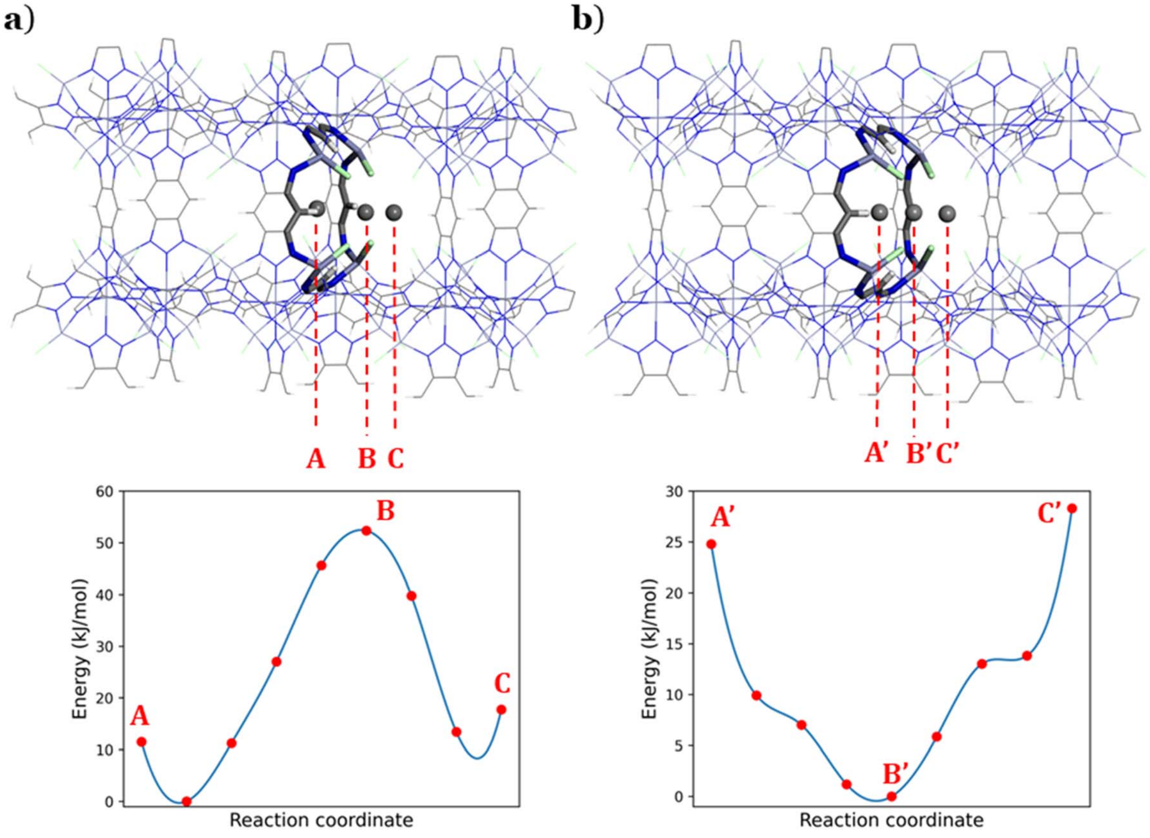

Fig. 2 Minimum-energy pathways for (a) CH_4 and (b) CO_2 migration across the pore gate (highlighted by thicker sticks) from the large cage to the small cage of MFU-4, obtained from DFT-based CINEB calculations. The molecules are represented only by their respective center of mass (carbon atom) for convenience of visualization. For CH_4, points A, B, and C represent the initial state, transition state, and final state, respectively. For CO_2, points A′, B′, and C′ correspond to the initial state, a local energy minimum at the pore gate, and the final state. In both cases, A (A′) lies within the large cage, B (B′) at the center of the pore gate, and C (C′) at the center of the smaller cage.

that MFU-4 can achieve size selective CO_2 adsorption over CH_4 *via* a predominantly kinetically controlled mechanism.

As a further step, we experimentally investigated the competitive adsorption of CO_2 and CH_4 under dynamic flow conditions. Accordingly, breakthrough experiments were performed for CO_2/CH_4 mixtures of 50 : 50 and 10 : 90 at total pressures of 100 and 500 kPa in the same range of temperature covered in the single-component adsorption measurements (see Table S7 for experimental conditions) under typical biogas upgrading conditions for PSA cyclic adsorption. These feed compositions provide a simple and industry-relevant reference condition, where the selected pressure interval reflects practical CO_2 capture and upgrading conditions of the feed to produce pure CH_4, near room temperature and at atmospheric to moderately elevated pressures relevant for cyclic PSA operation. It should be noted that, although raw biogas streams may contain trace contaminants such as H_2S and water, these species are typically removed during upstream conditioning, including desulfurization and dehydration steps (*e.g.*, guard beds). This is standard practice in commercial biogas upgrading systems, ensuring that the feed entering the adsorption unit is effectively dry and free of contaminants that could compromise the performance of the core process. In contrast to post-combustion streams, which are often treated directly under humid conditions, biogas streams are routinely pre-conditioned prior to separation.

Representative breakthrough curves for CO_2/CH_4 mixtures at 298 K are shown in Fig. 3. In all cases, CH_4 elutes almost immediately at the residence time of the gas in the column, indicating that the bulk CH_4 stream bypasses the adsorbent due to strong diffusional limitations as revealed by the DFT-derived MEPs. By contrast, CO_2 exhibits a clear and well-defined adsorption front, with the expected breakthrough around the stoichiometric time linked to the adsorption equilibrium concentration that relates to the feed saturation at equilibrium conditions. Moreover, the quantification of CO_2 loading from the mixture breakthrough curves (shown as empty markers in Fig. 1c) reveals that the CO_2 uptake under binary flow conditions closely matches the corresponding single-component values indicating, no competitive adsorption with CH_4. This one-to-one correspondence demonstrates that CH_4 does not effectively compete for adsorption sites, and CO_2 adsorption

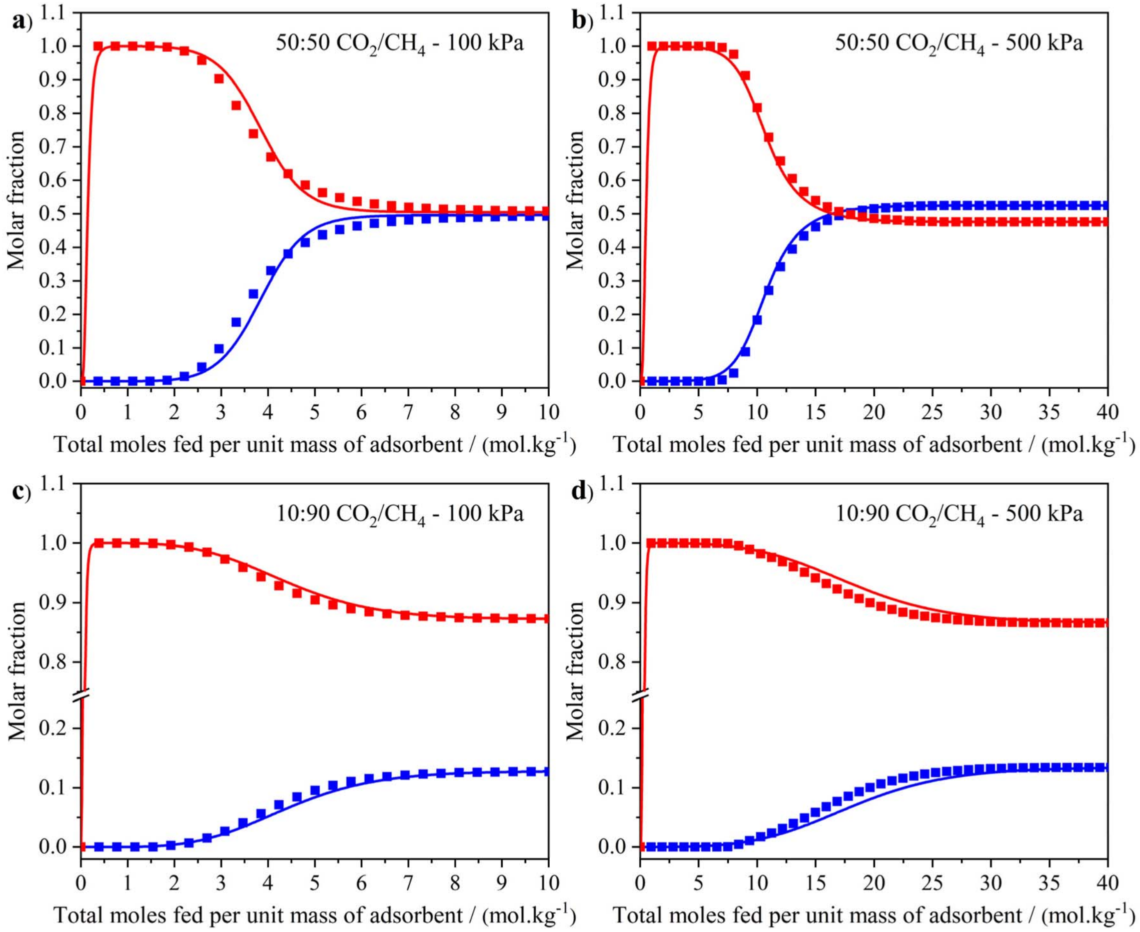

Fig. 3 CO_2/CH_4 binary mixtures breakthrough curves on MFU-4 at 298 K. Conditions for each panel are: (a) CO_2/CH_4 50 : 50 at 100 kPa, (b) CO_2/CH_4 50 : 50 at 500 kPa, (c) CO_2/CH_4 10 : 90 at 100 kPa, and (d) CO_2/CH_4 10 : 90 at 500 kPa. Data are plotted as component molar fraction (left *y*-axis) *versus* total moles fed per unit mass of adsorbent. Symbols represent experimental data, and continuous lines represent numerical simulations.

proceeds as if CH_4 were absent, a hallmark of a kinetically selective adsorption mechanism. Dilution of CO_2 in the feed from 50 : 50 to 10 : 90 has only a minor effect on the breakthrough profiles: the CO_2 front remains sharp and CH_4 continues to elute at the space time of the gas in the bed. Increasing the total pressure from 100 to 500 kPa proportionally enhances CO_2 uptake, consistent with the equilibrium isotherm, while leaving the kinetic exclusion of CH_4 unaffected. This kinetically selective behavior was confirmed by multiple adsorption/desorption cycles performed for a CO_2/CH_4 feed composition of 50 : 50 vol%, which yielded highly reproducible breakthrough curves (Fig. S15). The CO_2 adsorption capacity remained essentially unchanged over ten consecutive cycles, while CH_4 continued to behave as a non-adsorbing component, indicating the absence of CH_4 accumulation in the material and no loss of separation performance.

To further quantify the kinetic discrimination between CO_2 and CH_4, the breakthrough experiments were modeled using the Aspen Adsorption software, with the simulated profiles shown as continuous lines in Fig. 3. In these simulations, the mass-transfer coefficient of CH_4 ($k_{LDF}(CH_4)$) at 100 kPa was systematically varied to capture the experimentally observed inert-like behavior of CH_4 with MFU-4. The $k_{LDF}(CH_4)$ parameter was progressively reduced until agreement with the experimental breakthrough data was achieved. For $k_{LDF}(CH_4) \leq 1.0 \times 10^{-4}$ s^{-1}, the predicted CH_4 breakthrough curves become insensitive to further decreases in k_{LDF} and fully overlap with the experimental profiles, indicating that this value corresponds to a limiting diffusivity below which CH_4 breakthrough occurs essentially at the gas residence time in the fixed bed. By contrast, the CO_2 breakthrough curve profile is well reproduced with a $k_{LDF}(CO_2)$ value of 1.5×10^{-1} s^{-1}, which is approximately three orders of magnitude greater than the one for CH_4. This trend confirms that the transient column response is governed almost exclusively by CO_2 diffusion and adsorption inside the framework, while CH_4 behaves effectively as a dynamically non-adsorbing component, supporting that CO_2/CH_4 separation in MFU-4 is kinetically-governed giving rise to a molecular sieve separation of both components. Aspen Adsorption allows the k_{LDF} to incorporate combined temperature and pressure dependencies, following an Arrhenius-type expression for temperature and a first-order dependency on total pressure (eqn (S7)). Within this framework, the k_{LDF} coefficients employed for the breakthrough simulations at 500 kPa were obtained by scaling those determined at 100 kPa by a factor of five. Importantly, using the same $k_{LDF}(CO_2)/k_{LDF}(CH_4)$ ratio yields excellent agreement with the experimental breakthrough profiles at 500 kPa (Fig. 3b and d), demonstrating that the pronounced difference in diffusion kinetics between CO_2 and CH_4 is preserved at elevated pressure. This result further confirms that CO_2/CH_4 separation in MFU-4 remains kinetically governed under elevated pressure conditions relevant to industrial operation, with CH_4 continuing to behave as a dynamically non-adsorbing component.

Breakthrough curves at 313 and 343 K, together with their corresponding dynamic simulations, are equally provided in Fig. S13 and S14. Although increasing the temperature reduces the overall CO_2 uptake, the qualitative features of the breakthrough profiles remain unchanged: CH_4 elutes at the space time of the gas in the bed whereas CO_2 is selectively adsorbed. The numerical simulations accurately reproduce these experimental profiles, reinforcing the conclusion that MFU-4 maintains strong kinetic sieving behavior over a wide range of operating conditions relevant to natural gas upgrading and biogas purification strategies, especially by PSA. The full set of kinetic parameters for the CO_2 and CH_4 simulations (including k_∞, E_i, and k_{LDF} at each temperature and pressure) are provided in Table S8.

The performance of MFU-4 was evaluated against the two industrially established benchmark adsorbents CMS-3K and ETS-4, using CO_2 adsorption equilibrium uptake, kinetic selectivity (Habgood formulation, eqn (S10)) and working capacity (100–500 kPa, eqn (S11)) as key performance metrics. Fig. 4a reports the single component CO_2 adsorption isotherms for MFU-4 at near-ambient temperature and the same data reported previously for the benchmark adsorbents ion exchanged ETS-4 and CMS-3K. The comparison highlights that MFU-4 exhibits a much higher CO_2 uptake across the entire pressure range. In particular, MFU-4 reaches a CO_2 loading of ~7.4 mol kg^{-1} at 500 kPa, substantially exceeding the uptakes of CMS-3K, Ba-ETS-4 and Sr-ETS-4 which remain below 3.0 mol kg^{-1} over the same pressure range. This superior uptake directly translates into outstanding CO_2 working capacities for both (50 : 50) and (10 : 90) CO_2/CH_4 mixture feeds over the 100–500 kPa range at 298 K. For a (50 : 50) mixture, MFU-4 delivers a working capacity of 3.93 mol kg^{-1}, exceeding those of CMS-3K (0.94 mol kg^{-1}) and ETS-4 variants (<0.60 mol kg^{-1}) by more than fourfold and six-fold, respectively (Fig. 4b and c). Remarkably, even under the more demanding 10 : 90 feed composition, MFU-4 retains a high working capacity of 1.52 mol kg^{-1}, outperforming CMS-3K and ETS-4 by approximately two- to four-fold, highlighting its attractiveness under industrially relevant conditions.

Decisively, this exceptional CO_2 working capacity is coupled with an unprecedented level of kinetic selectivity. MFU-4 attains a kinetic selectivity of 67, outperforming Ba-ETS-4 and Sr-ETS-4 by approximately 90–150% and exceeding CMS-3K by more than 300% (see Table S9 for detailed values). Achieving such simultaneous superiority in both uptake swing and kinetic discrimination is extremely rare in microporous adsorbents and, to date, has not been realized by any industrial benchmarks. In existing technologies based on ETS-4 and CMS-3K, comparable working capacities can only be approached through vacuum-assisted regeneration, which substantially increases the energy penalty and operating costs of VPSA processes.

Beyond this direct comparison with industrial benchmarks, a broader evaluation against representative adsorbents reported for biogas upgrading, primarily governed by thermodynamic separation mechanisms, further highlights the distinctive performance of MFU-4 (see Table S10). In terms of CO_2 adsorption capacity, at 298 K and 100 kPa, MFU-4 exhibits an uptake of 3.61 mol kg^{-1}, which is higher than that of silica-based materials (~0.3–1.0 mol kg^{-1}),[88–90] periodic mesoporous organosilicas (PMOs, ~0.5–1.2 mol kg^{-1}),[91] pillared clays (~0.5–

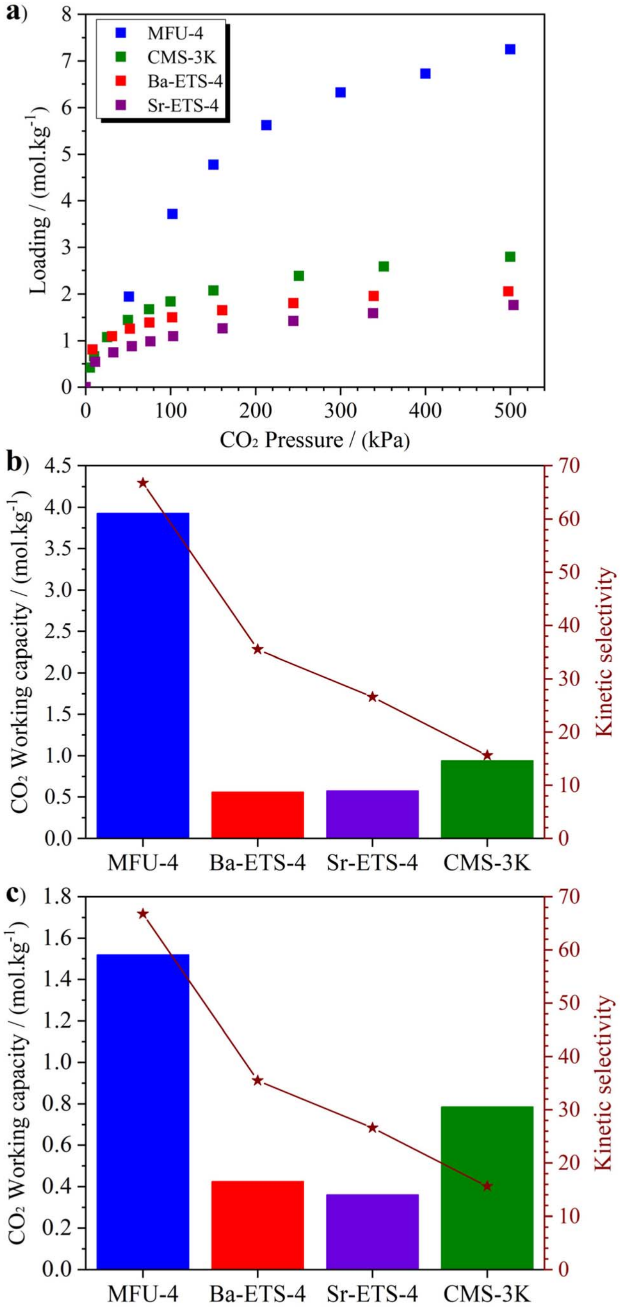

Fig. 4 Comparison of MFU-4 performance (this work) with benchmark adsorbents (ETS-4 variants,[54–56] CMS-3K[48]) for CO_2/CH_4 separation at near-ambient temperature. (a) Equilibrium single-component CO_2 adsorption isotherms at 298 K. (b–c) CO_2 working capacity *versus* kinetic selectivity for (b) 50 : 50 and (c) 10 : 90 CO_2/CH_4 mixtures.

1.5 mol kg^{-1}),[92] and typical activated carbons (~1.7–2.5 mol kg^{-1}).[93–96] With respect to other MOFs, MFU-4 shows a mixed uptake profile: it outperforms several materials, including MIL-101(Cr) (1.49 mol kg^{-1}),[97] IITKGP-21a (1.86 mol kg^{-1}),[98] CAU-10 (up to 2.3 mol kg^{-1}),[99] ZU-301 (2.41 mol kg^{-1}),[100] MIL-53 and MIL-125(Ti) (up to 2.64 mol kg^{-1}),[9,97,101] UiO-66(Zr) (up to 2.69 mol kg^{-1}),[101] and others,[102,103] while remaining comparable to MIL-100 (up to 3.5 mol kg^{-1}),[101] MIL-120(Al) (3.56 mol kg^{-1}),[43] and MIL-160(Al) (3.89 mol kg^{-1}).[104] However, lower CO_2 uptake is observed when compared to TAMOF-1,[105] ZJU-8a,[106] Cu-BTC,[101] UTSA-16/120,[107,108] SIFSIX-type materials,[108] with values collectively spanning 4.0–5.5 mol kg^{-1}, as well as Mg-MOF-74 (8.32 mol kg^{-1}),[36] known for its exceptional CO_2 adsorption capacity. A similar trend is observed for zeolites, where MFU-4 exhibits higher uptake than DDR (1.37 mol kg^{-1}),[109] Na-ZSM-5 (1.39 mol kg^{-1}),[110] silicalite-1 (1.69 mol kg^{-1}),[109] beta (2.05 mol kg^{-1}),[109] and 5A (3.06 mol kg^{-1}),[20] while remaining lower than 4A (4.29 mol kg^{-1}),[15] 13X (4.58 mol kg^{-1}),[7] NaX (4.82 mol kg^{-1}),[101] and NaY (5.44 mol kg^{-1}).[111] Importantly, at higher pressure (500 kPa), the experimental CO_2 uptake of MFU-4 reaches ~7.36 mol kg^{-1}, exceeding the capacity of several materials that outperform it at lower pressure, thereby highlighting its strong adsorption capability across the range relevant for practical applications. Under these conditions, In terms of CO_2 uptake, MFU-4 is only surpassed by a limited number of MOFs, such as ZJU-8a,[106] Cu-BTC,[101] and Mg-MOF-74,[36] with reported values ranging from 10.5 to 12.9 mol kg^{-1}.

In terms of adsorption energetics, MFU-4 presents a moderate CO_2 affinity (*i.e.* Q_{st} of 24.7 kJ mol^{-1}), which, relative to high-capacity MOFs, is comparable to that of ZJU-8a (19.5–21.9 kJ mol^{-1}),[106] while remaining significantly lower than that of Mg-MOF-74 (45.3–72.7 kJ mol^{-1}).[36] This further highlights the favorable balance between adsorption strength and regenerability of MFU-4. In terms of CO_2/CH_4 selectivity, MFU-4 exhibits a high value of 67 when evaluated using the Habgood formulation (eqn (S10)), a kinetic-based approach that integrates both equilibrium and kinetic contributions. This value already lies within the upper range of materials collected in Table S10. It is important to note that different approaches are commonly used to evaluate thermodynamic selectivity (see Section S3.2), leading to a wide range of reported values depending on the method employed. To enable a more consistent comparison with materials governed by equilibrium-based separation mechanisms, it is instructive to consider selectivity values derived from breakthrough experiments, which better reflect practical operating conditions. In this context, high selectivities for CO_2/CH_4 mixtures (~50 : 50 vol%) have been reported for materials such as zeolite 13X (88),[9] MIL-120 (89.3),[43] and NH_2-MIL-53(Al) (207)[9] at 100 kPa and 298–303 K. In the case of MFU-4, a fundamentally different behavior is observed. Breakthrough experiments reveal that CH_4 is effectively excluded from the framework due to severe diffusion limitations, resulting in negligible adsorption of this component. Consequently, when selectivity is evaluated directly from dynamic adsorption data, it can be considered essentially infinite for MFU-4.

Taken together, these results demonstrate that MFU-4 represents a step change in adsorbent performance for biogas upgrading, uniquely overcoming the long-standing trade-off between CO_2/CH_4 selectivity and uptake. By combining high working capacity, moderate adsorption energetics, and effectively infinite kinetic selectivity under dynamic conditions, MFU-4 enables high-efficiency separations without reliance on energy-intensive vacuum operation, setting it apart from both industrial benchmarks, such as CMS-3K and ETS-4, and state-of-the-art materials reported in the literature. Beyond separation performance, scalability and synthesis cost are critical considerations for industrial application. In this context, MFU-4 can be synthesized *via* relatively straightforward solvothermal methods using commercially available precursors, and its components are, in principle, amenable to scale-up. However, there are no detailed studies on the industrial scalability and the production cost of this MOF. As commonly observed in MOF chemistry, the cost associated with ligand and synthesis can be significantly reduced through the development of optimized synthetic routes and bulk production strategies.

4 Conclusions

In summary, we demonstrate that the ultra-microporous Zn triazolate MOF MFU-4 acts as an exceptionally efficient kinetic molecular sieve for CO_2/CH_4 separation, decisively outperforming industrial benchmark adsorbents such as CMS-3K and ion-exchanged ETS-4. Owing to its favorable architecture, which combines ultra-narrow pore gates with large cavities, MFU-4 uniquely delivers both high kinetic selectivity and high CO_2 working capacity, thereby explicitly breaking the long-standing trade-off between selectivity and uptake that constrains conventional molecular sieves. For a 50 : 50 CO_2/CH_4 mixture, MFU-4 achieves a CO_2 working capacity of 3.93 mol kg^{-1}, more than four and six times higher than CMS-3K (0.94 mol kg^{-1}) and ETS-4 variants (<0.60 mol kg^{-1}), respectively, while simultaneously reaching an exceptional kinetic selectivity of 67. This unprecedented combination enables efficient cyclic PSA operation over the industrially relevant 100–500 kPa pressure range without the need for vacuum-assisted regeneration. Together, these results establish MFU-4 as a showcase for the development of next-generation MOF adsorbent that redefines performance limits for energy-efficient biogas upgrading. Ongoing efforts should be now directed toward exploring alternative, more scalable synthesis approaches (*e.g.*, reflux-based methods) of MFU-4 to enable larger-scale production while maintaining material performance in order to facilitate its industrial translation.

Conflicts of interest

There are no conflicts to declare.

Data availability

Raw experimental and computational data and simulation files are available from the corrresponding authors upon reasonable request.

Supplementary information (SI): characterization of MFU-4; detailed description of the experimental and computational adsorption studies; additional experimental and computational results; benchmarking of MFU-4 against reported adsorbents. See DOI: https://doi.org/10.1039/d6ta01917j.

Acknowledgements

Adriano Henrique and José A. C. Silva acknowledge Portuguese national funds through FCT/MCTES (PIDDAC): CIMO UID/00690/2025 (https://doi.org/10.54499/UID/00690/2025) and UID/PRR/00690/2025 (https://doi.org/10.54499/UID/PRR/00690/2025); SusTEC, LA/P/0007/2020 (DOI: https://doi.org/10.54499/LA/P/0007/2020). Guillaume Maurin thanks Institut Universitaire de France for the Senior Chair.

References

1 I. Angelidaki, L. Treu, P. Tsapekos, G. Luo, S. Campanaro, H. Wenzel and P. G. Kougias, Biogas upgrading and utilization: Current status and perspectives, *Biotechnol. Adv.*, 2018, **36**, 452–466.
2 N. Scarlat, J. F. Dallemand and F. Fahl, Biogas: developments and perspectives in Europe, *Renewable Energy*, 2018, **129**, 457–472.
3 E. Ryckebosch, M. Drouillon and H. Vervaeren, Techniques for transformation of biogas to biomethane, *Biomass Bioenergy*, 2011, **35**, 1633–1645.
4 B. Aghel, S. Behaein, S. Wongwises and M. S. Shadloo, A review of recent progress in biogas upgrading: with emphasis on carbon capture, *Biomass Bioenergy*, 2022, **160**, 106422.
5 A. A. Abd, M. R. Othman, Z. Helwani and J. Kim, Waste to wheels: performance comparison between pressure swing adsorption and amine-absorption technologies for upgrading biogas containing hydrogen sulfide to fuel grade standards, *Energy*, 2023, **272**, 127060.
6 A. Ali Abd, M. Roslee Othman, Z. Helwani and J. Kim, An overview of biogas upgrading via pressure swing adsorption: Navigating through bibliometric insights towards a conceptual framework and future research pathways, *Energy Convers. Manag.*, 2024, **306**, 118268.
7 S. Cavenati, C. A. Grande and A. E. Rodrigues, Adsorption equilibrium of methane, carbon dioxide, and nitrogen on zeolite 13X at high pressures, *J. Chem. Eng. Data*, 2004, **49**, 1095–1101.
8 J. A. C. Silva, K. Schumann and A. E. Rodrigues, Sorption and kinetics of CO_2 and CH_4 in binderless beads of 13X zeolite, *Microporous Mesoporous Mater.*, 2012, **158**, 219–228.
9 S. A. Peter, G. V. Baron, J. Gascon, F. Kapteijn and J. F. M. Denayer, Dynamic desorption of CO_2 and CH_4 from amino-MIL-53(Al) adsorbent, *Adsorption*, 2013, **19**, 1235–1244.
10 J. A. C. Silva, A. F. Cunha, K. Schumann and A. E. Rodrigues, Binary adsorption of CO_2/CH_4 in binderless beads of 13X zeolite, *Microporous Mesoporous Mater.*, 2014, **187**, 100–107.
11 C. A. Grande and R. Blom, Cryogenic adsorption of methane and carbon dioxide on zeolites 4A and 13X, *Energy Fuels*, 2014, **28**, 6688–6693.
12 F. A. Abdul Kareem, A. M. Shariff, S. Ullah, N. Mellon and L. K. Keong, Adsorption of pure and predicted binary (CO2:CH4) mixtures on 13X-zeolite: equilibrium and

kinetic properties at offshore conditions, *Microporous Mesoporous Mater.*, 2018, **267**, 221–234.

13 A. Streb and M. Mazzotti, Adsorption for efficient low carbon hydrogen production: part 1-adsorption equilibrium and breakthrough studies for $H_2/CO_2/CH_4$ on zeolite 13X, *Adsorption*, 2021, **27**, 541–558.

14 H. Jedli, S. M. Bouzgarrou, R. Hassani, E. Sabi and K. Slimi, Adsorption of CO_2, CH_4 and H_2 onto zeolite 13 X: Kinetic and equilibrium studies, *Heliyon*, 2024, **10**, e40672.

15 K. G. Wynnyk, B. Hojjati, P. Pirzadeh and R. A. Marriott, High-pressure sour gas adsorption on zeolite 4A, *Adsorption*, 2017, **23**, 149–162.

16 R. Seabra, A. M. Ribeiro, K. Gleichmann, A. F. P. Ferreira and A. E. Rodrigues, Adsorption equilibrium and kinetics of carbon dioxide, methane and nitrogen on binderless zeolite 4A adsorbents, *Microporous Mesoporous Mater.*, 2019, **277**, 105–114.

17 L. F. A. S. Zafanelli, A. Henrique, M. Karimi, A. E. Rodrigues and J. A. C. Silva, Single- and multicomponent fixed bed adsorption of CO_2, CH_4, and N_2 in binder-Free beads of 4A zeolite, *Ind. Eng. Chem. Res.*, 2020, **59**, 13724–13734.

18 S. Duan, Y. Xie, H. Yin and P. Shen, Investigation of CO_2, CH_4 and N_2 adsorption mechanism on zeolite 4A using statistical physics and site energy distribution analysis, *Microporous Mesoporous Mater.*, 2025, **398**, 113826.

19 D. Saha, Z. Bao, F. Jia and S. Deng, Adsorption of CO_2, CH_4, N_2O, and N_2 on MOF-5, MOF-177, and zeolite 5A, *Environ. Sci. Technol.*, 2010, **44**, 1820–1826.

20 M. Mofarahi and F. Gholipour, Gas adsorption separation of CO_2/CH_4 system using zeolite 5A, *Microporous Mesoporous Mater.*, 2014, **200**, 1–10.

21 M. I. Hossain, B. D. Rabideau and T. G. Glover, The impact of trace amounts of CO_2 on the high-pressure adsorption of CH_4 on 5A zeolite, *Microporous Mesoporous Mater.*, 2024, **369**, 112948.

22 S. R. Jeong, K. M. Kim and C. H. Lee, Adsorption equilibria and kinetics of CO_2, CO, CH_4, N_2, and H_2 on zeolite 5 A up to 1.0 MPa, *Chem. Eng. J.*, 2025, **525**, 170014.

23 X. Xu, X. Zhao, L. Sun and X. Liu, Adsorption separation of carbon dioxide, methane, and nitrogen on Hβ and Na-exchanged β-zeolite, *J. Nat. Gas Chem.*, 2008, **17**, 391–396.

24 J. Yang, Q. Zhao, H. Xu, L. Li, J. Dong and J. Li, Adsorption of CO_2, CH_4, and N_2 on gas diameter grade ion-exchange small pore zeolites, *J. Chem. Eng. Data*, 2012, **57**, 3701–3709.

25 Y. Li, H. Yi, X. Tang, F. Li and Q. Yuan, Adsorption separation of CO_2/CH_4 gas mixture on the commercial zeolites at atmospheric pressure, *Chem. Eng. J.*, 2013, **229**, 50–56.

26 P. A. S. Moura, D. P. Bezerra, E. Vilarrasa-Garcia, M. Bastos-Neto and D. C. S. Azevedo, Adsorption equilibria of CO_2 and CH_4 in cation-exchanged zeolites 13X, *Adsorption*, 2016, **22**, 71–80.

27 H. Golipour, B. Mokhtarani, M. Mafi, M. Khadivi and H. R. Godini, Systematic measurements of CH_4 and CO_2 adsorption isotherms on cation-exchanged zeolites 13X, *J. Chem. Eng. Data*, 2019, **64**, 4412–4423.

28 H. Golipour, B. Mokhtarani, M. Mafi, M. Khadivi and H. R. Godini, Systematic Measurements of CH4 and CO_2 Adsorption Isotherms on Cation-Exchanged Zeolites 13X, *J. Chem. Eng. Data*, 2019, **64**, 4412–4423.

29 L. Feng, Y. Shen, T. Wu, B. Liu, D. Zhang and Z. Tang, Adsorption equilibrium isotherms and thermodynamic analysis of CH_4, CO_2, CO, N_2 and H_2 on NaY Zeolite, *Adsorption*, 2020, **26**, 1101–1111.

30 E. Aly, L. F. A. S. Zafanelli, A. Henrique, M. Golini Pires, A. E. Rodrigues, K. Gleichmann and J. A. C. Silva, Fixed bed adsorption of CO_2, CH_4, and N_2 and their mixtures in potassium-exchanged binder-free beads of Y zeolite, *Ind. Eng. Chem. Res.*, 2021, **60**, 15236–15247.

31 A. M. Najafi, F. Khorasheh, S. Soltanali and H. Ghassabzadeh, Equilibrium and kinetic insights into the comprehensive investigation of CO_2, CH_4, and N_2 adsorption on cation-exchanged X and Y faujasite zeolites, *Langmuir*, 2023, **39**, 15535–15546.

32 Y. Sun, H. Li, H. Lai, Y. Yu, M. Hou, C. Fu, Z. Wang and C. Zhang, CO_2 selective adsorption from CO_2/CH_4 mixtures and regeneration of X zeolites by Li and K modification using various regeneration strategies, *Chem. Eng. J.*, 2025, **515**, 163682.

33 B. Achenbach, A. Yurdusen, N. Stock, G. Maurin and C. Serre, Synthetic aspects and characterization needs in MOF chemistry – from discovery to applications, *Adv. Mater.*, 2025, 2411359.

34 S. R. Caskey, A. G. Wong-Foy and A. J. Matzger, Dramatic tuning of carbon dioxide uptake via metal substitution in a coordination polymer with cylindrical pores, *J. Am. Chem. Soc.*, 2008, **130**, 10870–10871.

35 J. A. Mason, K. Sumida, Z. R. Herm, R. Krishna and J. R. Long, Evaluating metal-organic frameworks for post-combustion carbon dioxide capture via temperature swing adsorption, *Energy Environ. Sci.*, 2011, **4**, 3030–3040.

36 Z. Bao, L. Yu, Q. Ren, X. Lu and S. Deng, Adsorption of CO_2 and CH_4 on a magnesium-based metal organic framework, *J. Colloid Interface Sci.*, 2011, **353**, 549–556.

37 T. M. McDonald, W. R. Lee, J. A. Mason, B. M. Wiers, C. S. Hong and J. R. Long, Capture of carbon dioxide from air and flue gas in the alkylamine-appended metal-organic framework mmen-Mg_2(dobpdc), *J. Am. Chem. Soc.*, 2012, **134**, 7056–7065.

38 T. M. McDonald, J. A. Mason, X. Kong, E. D. Bloch, D. Gygi, A. Dani, V. Crocellà, F. Giordanino, S. O. Odoh, W. S. Drisdell, B. Vlaisavljevich, A. L. Dzubak, R. Poloni, S. K. Schnell, N. Planas, K. Lee, T. Pascal, L. F. Wan, D. Prendergast, J. B. Neaton, B. Smit, J. B. Kortright, L. Gagliardi, S. Bordiga, J. A. Reimer and J. R. Long, Cooperative insertion of CO_2 in diamine-appended metal-organic frameworks, *Nature*, 2015, **519**, 303–308.

39 W. R. Lee, H. Jo, L. M. Yang, H. Lee, D. W. Ryu, K. S. Lim, J. H. Song, D. Y. Min, S. S. Han, J. G. Seo, Y. K. Park, D. Moon and C. S. Hong, Exceptional CO_2 working capacity in a heterodiamine-grafted metal-organic framework, *Chem. Sci.*, 2015, **6**, 3697–3705.

40 E. J. Kim, R. L. Siegelman, H. Z. H. Jiang, A. C. Forse, J. H. Lee, J. D. Martell, P. J. Milner, J. M. Falkowski, J. B. Neaton, J. A. Reimer, S. C. Weston and J. R. Long, Cooperative carbon capture and steam regeneration with tetraamine-appended metal-organic frameworks, *Science*, 2020, **369**, 392–396.

41 R. P. Loughran, T. Hurley, A. Gładysiak, A. Chidambaram, K. Khivantsev, E. D. Walter, T. R. Graham, P. Reardon, J. Szanyi, D. B. Fast, Q. R. S. Miller, A. H. A. Park and K. C. Stylianou, CO_2 capture from wet flue gas using a water-stable and cost-effective metal-organic framework, *Cell Rep. Phys. Sci.*, 2023, **4**, 101470.

42 B. Chen, D. Fan, R. V. Pinto, I. Dovgaliuk, S. Nandi, D. Chakraborty, N. García-Moncada, A. Vimont, C. J. McMonagle, M. Bordonhos, A. Al Mohtar, I. Cornu, P. Florian, N. Heymans, M. Daturi, G. De Weireld, M. Pinto, F. Nouar, G. Maurin, G. Mouchaham and C. Serre, A scalable robust microporous Al-MOF for post-combustion carbon capture, *Adv. Sci.*, 2024, **11**, 2401070.

43 M. Bordonhos, R. V. Pinto, T. Frade, B. Chen, F. Nouar, G. Mouchaham, J. R. B. Gomes, C. Serre and M. L. Pinto, Towards sustainable biogas upgrading: MIL-120(Al) as a cost-effective water stable MOF for CO_2/CH_4 separation, *J. Mater. Chem. A*, 2026, **14**, 12856–12866.

44 J.-B. Lin, T. T. T. Nguyen, R. Vaidhyanathan, J. Burner, J. M. Taylor, H. Durekova, F. Akhtar, R. K. Mah, O. Ghaffari-Nik, S. Marx, N. Fylstra, S. S. Iremonger, K. W. Dawson, P. Sarkar, P. Hovington, A. Rajendran, T. K. Woo and G. K. H. Shimizu, A scalable metal-organic framework as a durable physisorbent for carbon dioxide capture, *Science*, 2021, **374**, 1464–1469.

45 P. M. Bhatt, Y. Belmabkhout, A. Cadiau, K. Adil, O. Shekhah, A. Shkurenko, L. J. Barbour and M. Eddaoudi, A fine-tuned fluorinated MOF addresses the needs for trace CO_2 removal and air capture using physisorption, *J. Am. Chem. Soc.*, 2016, **138**, 9301–9307.

46 D. M. Ruthven, *Principles of Adsorption and Adsorption Processes*, John Wiley & Sons, 1984.

47 R. T. Yang, *Adsorbents: Fundamentals and Applications*, John Wiley & Sons, 2003.

48 S. Cavenati, *Separação de Misturas $CH_4/CO_2/N_2$ Por Processos Adsorptivos*, Faculdade de Engenharia da Universidade do Porto, 2005.

49 S. Cavenati, C. A. Grande and A. E. Rodrigues, Upgrade of methane from landfill gas by pressure swing adsorption, *Energy Fuels*, 2005, **19**, 2545–2555.

50 SysAdvance, *Energy – Biogas Upgrading | H2S Reduction (Technical Brochure)*, 2023.

51 SysAdvance, *Industrial – Nitrogen Series | Oxygen Series | Helisys | OxygenVSA (Technical Brochure)*, 2023.

52 S. M. Kuznicki, *US Pat.*, 4938939, 1990.

53 S. M. Kuznicki, V. A. Bell, S. Nair, H. W. Hillhouse, R. M. Jacubinas, C. M. Braunbarth, B. H. Toby and M. Tsapatsis, A titanosilicate molecular sieve with adjustable pores for size-selective adsorption of molecules, *Nature*, 2001, **412**, 720–724.

54 R. P. Marathe, S. Farooq and M. P. Srinivasan, Modeling gas adsorption and transport in small-pore titanium silicates, *Langmuir*, 2005, **21**, 4532–4546.

55 B. Majumdar, S. J. Bhadra, R. P. Marathe and S. Farooq, Adsorption and diffusion of methane and nitrogen in barium exchanged ETS-4, *Ind. Eng. Chem. Res.*, 2011, **50**, 3021–3034.

56 Q. Peng, Y. Chen, D. Fang, C. Liu, K. Wu, Y. Chen, H. Jiang, Y. Sun, Q. Wu, D. Wu and H. Sun, Enhancing size-selective adsorption of CO_2/CH_4 on ETS-4 via ion-exchange coupled with thermal treatment, *Ind. Eng. Chem. Res.*, 2023, **62**, 9313–9324.

57 Guild Associates, Molecular Gate® Adsorbent Technology, can be found under https://www.guildassociates.com/gas-processing-systems/mgtech/.

58 M. Azadi Tabar, E. Pancione, S. A. Peter and J. F. M. Denayer, Four-column vacuum pressure swing adsorption for biogas upgrading with co-production of high-purity biogenic CO2: experimental and simulation study, *J. CO_2 Util.*, 2026, **105**, 103348.

59 S. Biswas, M. Grzywa, H. P. Nayek, S. Dehnen, I. Senkovska, S. Kaskel and D. Volkmer, A cubic coordination framework constructed from benzobistriazolate ligands and zinc ions having selective gas sorption properties, *Dalton Trans.*, 2009, 6487–6495.

60 H. Hart and D. Ok, Synthesis of 1,5-diamino-1,5-dihydrobenzo[1,2-d:4,5-d']bistriazole (DABT) and its use as a 1,4-benzadiyne equivalent, *J. Org. Chem.*, 1986, **51**, 979–986.

61 Aspentech, *Aspen AdsimTM 11.1 – Adsorption Reference Guide*, Cambridge, 2001.

62 D. D. Do, *Adsorption Analysis: Equilibria and Kinetics*, Imperial College Press, 1998.

63 S. Sircar and J. R. Hufton, Why does the linear driving force model for adsorption kinetics work?, *Adsorption*, 2000, **6**, 137–147.

64 A. Henrique, A. E. Rodrigues and J. A. C. Silva, Separation of hexane isomers in ZIF-8 by fixed bed adsorption, *Ind. Eng. Chem. Res.*, 2019, **58**, 378–394.

65 A. Henrique, A. E. Rodrigues and J. A. C. Silva, Fixed bed dynamics of single and multicomponent adsorption of pentane and hexane isomers in ZIF-8, *Sep. Purif. Technol.*, 2020, **238**, 116419.

66 G. Kresse and J. Furthmüller, Efficient iterative schemes for ab initio total-energy calculations using a plane-wave basis set, *Phys. Rev. B: Condens. Matter Mater. Phys.*, 1996, **54**, 11169–11186.

67 J. P. Perdew, K. Burke and M. Ernzerhof, Generalized gradient approximation made simple, *Phys. Rev. Lett.*, 1996, **77**, 3865–3868.

68 P. E. Blochl, Projector augmented-wave method, *Phys. Rev. B: Condens. Matter Mater. Phys.*, 1994, **50**, 17953–17979.

69 S. Grimme, Semiempirical GGA-type density functional constructed with a long-range dispersion correction, *J. Comput. Chem.*, 2006, **27**, 1787–1799.

70 S. Grimme, S. Ehrlich and L. Goerigk, Effect of the damping function in dispersion corrected density functional theory, *J. Comput. Chem.*, 2011, **32**, 1456–1465.

71 H. J. Monkhorst and J. D. Pack, Special points for Brillouin-zone integrations, *Phys. Rev. B*, 1976, **13**, 5188–5192.

72 T. A. Manz and N. G. Limas, Introducing DDEC6 atomic population analysis: Part 1. Charge partitioning theory and methodology, *RSC Adv.*, 2016, **6**, 47771–47801.

73 N. G. Limas and T. A. Manz, Introducing DDEC6 atomic population analysis: Part 2. Computed results for a wide range of periodic and nonperiodic materials, *RSC Adv.*, 2016, **6**, 45727–45747.

74 T. A. Manz, Introducing DDEC6 atomic population analysis: Part 3. Comprehensive method to compute bond orders, *RSC Adv.*, 2017, **7**, 45552–45581.

75 N. G. Limas and T. A. Manz, Introducing DDEC6 atomic population analysis: Part 4. Efficient parallel computation of net atomic charges, atomic spin moments, bond orders, and more, *RSC Adv.*, 2018, **8**, 2678–2707.

76 J. G. Harris and K. H. Yungt, Carbon dioxide's liquid-vapor coexistence curve and critical properties as predicted by a simple molecular model, *J. Phys. Chem.*, 1995, **99**, 12021–12024.

77 M. G. Martin and J. I. Siepmann, Transferable potentials for phase equilibria. 1. United-atom description of n-alkanes, *J. Phys. Chem. B*, 1998, **102**, 2569–2577.

78 A. K. Rappé, C. J. Casewit, K. S. Colwell, W. A. Goddard and W. M. Skiff, UFF, a full periodic table force field for molecular mechanisms and molecular dynamics simulations, *J. Am. Chem. Soc.*, 1992, **114**, 10024–10035.

79 Q. Yang and C. Zhong, Molecular simulation of carbon dioxide/methane/hydrogen mixture adsorption in metal-organic frameworks, *J. Phys. Chem. B*, 2006, **110**, 17776–17783.

80 T. J. H. Vlugt, E. García-Pérez, D. Dubbeldam, S. Ban and S. Calero, Computing the heat of adsorption using molecular simulations: The effect of strong Coulombic interactions, *J. Chem. Theory Comput.*, 2008, **4**, 1107–1118.

81 G. Henkelman, B. P. Uberuaga and H. Jónsson, A climbing image nudged elastic band method for finding saddle points and minimum energy paths, *J. Chem. Phys.*, 2000, **113**, 9901–9904.

82 T. D. Kühne, M. Iannuzzi, M. Del Ben, V. V. Rybkin, P. Seewald, F. Stein, T. Laino, R. Z. Khaliullin, O. Schütt, F. Schiffmann, D. Golze, J. Wilhelm, S. Chulkov, M. H. Bani-Hashemian, V. Weber, U. Borštnik, M. Taillefumier, A. S. Jakobovits, A. Lazzaro, H. Pabst, T. Müller, R. Schade, M. Guidon, S. Andermatt, N. Holmberg, G. K. Schenter, A. Hehn, A. Bussy, F. Belleflamme, G. Tabacchi, A. Glöß, M. Lass, I. Bethune, C. J. Mundy, C. Plessl, M. Watkins, J. VandeVondele, M. Krack and J. Hutter, CP2K: An electronic structure and molecular dynamics software package - Quickstep: Efficient and accurate electronic structure calculations, *J. Chem. Phys.*, 2020, **152**, 194103.

83 J. VandeVondele and J. Hutter, Gaussian basis sets for accurate calculations on molecular systems in gas and condensed phases, *J. Chem. Phys.*, 2007, **127**, 144105.

84 S. Goedecker, M. Teter and J. Hutter, Separable dual-space Gaussian pseudopotentials, *Phys. Rev. B: Condens. Matter Mater. Phys.*, 1996, **54**, 1703–1710.

85 M. Krack, Pseudopotentials for H to Kr optimized for gradient-corrected exchange-correlation functionals, *Theor. Chem. Acc.*, 2005, **114**, 145–152.

86 M. Thommes, K. Kaneko, A. V. Neimark, J. P. Olivier, F. Rodriguez-Reinoso, J. Rouquerol and K. S. W. Sing, Physisorption of gases, with special reference to the evaluation of surface area and pore size distribution (IUPAC technical report), *Pure Appl. Chem.*, 2015, **87**, 1051–1069.

87 G. Sastre, J. Van Den Bergh, F. Kapteijn, D. Denysenko and D. Volkmer, Unveiling the mechanism of selective gate-driven diffusion of CO_2 over N_2 in MFU-4 metal-organic framework, *Dalton Trans.*, 2014, **43**, 9612–9619.

88 Y. Belmabkhout and A. Sayari, Adsorption of CO2 from dry gases on MCM-41 silica at ambient temperature and high pressure. 2: Adsorption of CO_2/N_2, CO_2/CH_4 and CO_2/H_2 binary mixtures, *Chem. Eng. Sci.*, 2009, **64**, 3729–3735.

89 L. Mafra, T. Čendak, S. Schneider, P. V. Wiper, J. Pires, J. R. B. Gomes and M. L. Pinto, Amine functionalized porous silica for CO_2/CH_4 separation by adsorption: Which amine and why, *Chem. Eng. J.*, 2018, **336**, 612–621.

90 M. Pacheco, M. Bordonhos, M. Sardo, R. Afonso, J. R. B. Gomes, L. Mafra and M. L. Pinto, Moisture effect on the separation of CO_2/CH_4 mixtures with amine-functionalised porous silicas, *Chem. Eng. J.*, 2022, **443**, 136271.

91 M. A. O. Lourenço, C. Siquet, M. Sardo, L. Mafra, J. Pires, M. Jorge, M. L. Pinto, P. Ferreira and J. R. B. Gomes, Interaction of CO2 and CH4 with functionalized periodic mesoporous phenylene-silica: periodic DFT calculations and gas adsorption measurements, *J. Phys. Chem. C*, 2016, **120**, 3863–3875.

92 J. Pires, V. K. Saini and M. L. Pinto, Studies on selective adsorption of biogas components on pillared clays: Approach for biogas improvement, *Environ. Sci. Technol.*, 2008, **42**, 8727–8732.

93 C. A. Grande, R. Blom, A. Möller and J. Möllmer, High-pressure separation of CH_4/CO_2 using activated carbon, *Chem. Eng. Sci.*, 2013, **89**, 10–20.

94 N. Álvarez-Gutiérrez, M. V. Gil, F. Rubiera and C. Pevida, Adsorption performance indicators for the CO_2/CH_4 separation: Application to biomass-based activated carbons, *Fuel Process. Technol.*, 2016, **142**, 361–369.

95 N. Álvarez-Gutiérrez, S. García, M. V. Gil, F. Rubiera and C. Pevida, Dynamic performance of biomass-based carbons for CO_2/CH_4 separation. Approximation to a pressure swing adsorption process for biogas upgrading, *Energy Fuels*, 2016, **30**, 5005–5015.

96 I. Durán, N. Álvarez-Gutiérrez, F. Rubiera and C. Pevida, Biogas purification by means of adsorption on pine

sawdust-based activated carbon: Impact of water vapor, *Chem. Eng. J.*, 2018, **353**, 197–207.

97 N. Singh, S. Dalakoti, A. Sharma, R. Chauhan, R. S. Murali, S. Divekar, S. Dasgupta and Aarti, Shaping of MIL-53-Al and MIL-101 MOF for CO_2/CH_4, CO_2/N_2 and CH_4/N_2 separation, *Sep. Purif. Technol.*, 2024, **341**, 126820.

98 R. Sahoo, B. Pramanik, R. Krishna and M. C. Das, A chemically robust 3D interpenetrated MOF toward one-step methane purification along with six other multipurpose gas separations, *Small*, 2026, **22**, e72629.

99 A. D. Wiersum, C. Giovannangeli, D. Vincent, E. Bloch, H. Reinsch, N. Stock, J. S. Lee, J. S. Chang and P. L. Llewellyn, Experimental screening of porous materials for high pressure gas adsorption and evaluation in gas separations: application to MOFs (MIL-100 and CAU-10), *ACS Comb. Sci.*, 2013, **15**, 111–119.

100 C. Yu, Q. Ding, J. Hu, Q. Wang, X. Cui and H. Xing, Selective capture of carbon dioxide from humid gases over a wide temperature range using a robust metal–organic framework, *Chem. Eng. J.*, 2021, **405**, 126937.

101 A. D. Wiersum, J. S. Chang, C. Serre and P. L. Llewellyn, An adsorbent performance indicator as a first step evaluation of novel sorbents for gas separations: application to metal-organic frameworks, *Langmuir*, 2013, **29**, 3301–3309.

102 D. Lv, R. Shi, Y. Chen, Y. Chen, H. Wu, X. Zhou, H. Xi, Z. Li and Q. Xia, Selective adsorptive separation of CO2/CH4 and CO2/N2 by a water resistant zirconium-porphyrin metal-organic framework, *Ind. Eng. Chem. Res.*, 2018, **57**, 12215–12224.

103 H. N. Wamba, S. Dalakoti, N. Singh, S. Divekar, J. Ngoune, A. Arya and S. Dasgupta, Facile aqueous medium synthesis of highly stable Zr-MOFs with promising CO_2/CH_4 adsorption selectivity for natural gas and biogas upgradation, *Ind. Eng. Chem. Res.*, 2023, **62**, 19773–19783.

104 M. Bordonhos, M. I. S. Neves, A. Marandi, F. Nouar, M. Jorge, J. R. B. Gomes, C. Serre and M. L. Pinto, Spanning the molecular to industrial scale of the adsorption-based separation of CO_2/CH_4 by MIL-160(Al), *Chem. Eng. J.*, 2025, **524**, 169276.

105 S. Capelo-Avilés, M. de Fez-Febré, S. R. G. Balestra, J. Cabezas-Giménez, R. Tomazini de Oliveira, I. I. Gallo Stampino, A. Vidal-Ferran, J. González-Cobos, V. Lillo, O. Fabelo, E. C. Escudero-Adán, L. R. Falvello, J. B. Parra, P. Rumori, G. Turnes Palomino, C. Palomino Cabello, S. Giancola, S. Calero and J. R. Galán-Mascarós, Selective adsorption of CO2 in TAMOF-1 for the separation of CO_2/CH_4 gas mixtures, *Nat. Commun.*, 2025, **16**, 3243.

106 J. Cai, H. Wang, H. Wang, X. Duan, Z. Wang, Y. Cui, Y. Yang, B. Chen and G. Qian, An amino-decorated NbO-type metal-organic framework for high C_2H_2 storage and selective CO2 capture, *RSC Adv.*, 2015, **5**, 77417–77422.

107 S. Xiang, Y. He, Z. Zhang, H. Wu, W. Zhou, R. Krishna and B. Chen, Microporous metal-organic framework with potential for carbon dioxide capture at ambient conditions, *Nat. Commun.*, 2012, **3**, 954.

108 H. M. Wen, C. Liao, L. Li, A. Alsalme, Z. Alothman, R. Krishna, H. Wu, W. Zhou, J. Hu and B. Chen, A metal-organic framework with suitable pore size and dual functionalities for highly efficient post-combustion CO_2 capture, *J. Mater. Chem. A*, 2019, **7**, 3128–3134.

109 J. Yang, J. Li, W. Wang, L. Li and J. Li, Adsorption of CO_2, CH_4, and N_2 on 8-, 10-, and 12-membered ring hydrophobic microporous high-silica zeolites: DDR, Silicalite-1, and Beta, *Ind. Eng. Chem. Res.*, 2013, **52**, 17856–17864.

110 M. Rahmani, B. Mokhtarani, M. Mafi and N. Rahmanian, Acid gas removal by superhigh silica ZSM-5: adsorption isotherms of hydrogen sulfide, carbon dioxide, methane, and nitrogen, *Ind. Eng. Chem. Res.*, 2022, **61**, 6600–6610.

111 A. Sharma, A. Verma, U. Kumar, N. Singh, S. Dalakoti, R. Chauhan, S. Bhandari, S. Divekar, S. Dasgupta and Aarti, Interchangeable effect of polyols-based zeolite on the separation of CO_2, CH_4, and N_2 gases, *Microporous Mesoporous Mater.*, 2024, **367**, 112984.